

RESEARCH ARTICLE | AUGUST 04 2023

Excitonic and deep-level emission from N- and Al-polar homoepitaxial AlN grown by molecular beam epitaxy

L. van Deurzen ; J. Singhal ; J. Encomendero ; N. Pieczulewski ; C. S. Chang ; Y. Cho ; D. A. Muller ; H. G. Xing ; D. Jena ; O. Brandt ; J. Lähnemann 

 Check for updates

APL Mater 11, 081109 (2023)

<https://doi.org/10.1063/5.0158390>



View Online

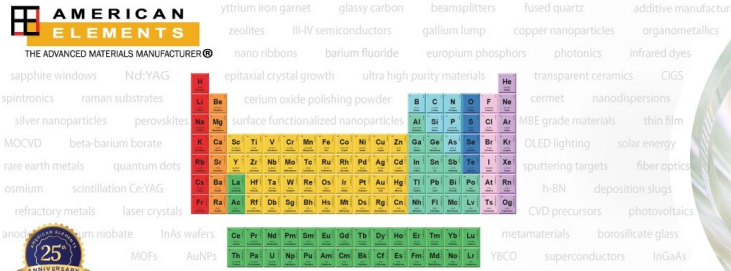


Export Citation

CrossMark

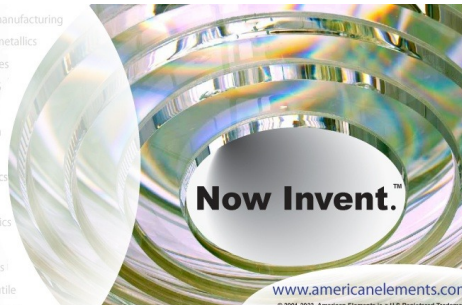
07 August 2023 07:50:55

AMERICAN ELEMENTS
THE ADVANCED MATERIALS MANUFACTURER®



yttrium iron garnet, zeolites, nano ribbons, epitaxial crystal growth, cerium oxide polishing powder, surface functionalized nanoparticles, refractory metals, laser crystals, anodic titanium niobate, InAs wafers, ZnS, CdTe, perovskite crystals, transparent ceramics

glassy carbon, beamsplitters, fused quartz, additive manufacturing, organometallics, copper nanoparticles, infrared dyes, ultra high purity materials, transparent ceramics, CIGS, MBE grade materials, thin film, OLED lighting, solar energy, sputtering targets, fiber optics, h-BN, deposition slugs, CVD precursors, photovoltaics, metamaterials, borosilicate glass, YBCO superconductors, InGaAs, indium tin oxide, MgF2, rutile, diamond micropowder, optical glass



Now Invent.™

www.americanelements.com

© 2001-2022, American Elements LLC, a U.S. Registered Trademark.

The Next Generation of Material Science Catalogs

Excitonic and deep-level emission from N- and Al-polar homoepitaxial AlN grown by molecular beam epitaxy

Cite as: APL Mater. 11, 081109 (2023); doi: 10.1063/5.0158390

Submitted: 16 May 2023 • Accepted: 19 July 2023 •

Published Online: 4 August 2023



View Online



Export Citation



CrossMark

L. van Deurzen,^{1,a)} J. Singhal,² J. Encomendero,² N. Pieczulewski,³ C. S. Chang,^{1,4} Y. Cho,² D. A. Muller,^{1,5} H. G. Xing,^{2,3,5} D. Jena,^{1,2,3,5} O. Brandt,⁶ and J. Lähnemann⁶

AFFILIATIONS

¹School of Applied and Engineering Physics, Cornell University, Ithaca, New York 14853, USA

²Department of Electrical and Computer Engineering, Cornell University, Ithaca, New York 14853, USA

³Department of Materials Science and Engineering, Cornell University, Ithaca, New York 14853, USA

⁴Research Laboratory of Electronics, Massachusetts Institute of Technology, Cambridge, Massachusetts 02139, USA

⁵Kavli Institute at Cornell for Nanoscale Science, Cornell University, Ithaca, New York 14853, USA

⁶Paul-Drude-Institut für Festkörperelektronik, Leibniz-Institut im Forschungsverbund Berlin e.V., 10117 Berlin, Germany

^{a)} Author to whom correspondence should be addressed: lhv9@cornell.edu

ABSTRACT

Using low-temperature cathodoluminescence spectroscopy, we study the properties of N- and Al-polar AlN layers grown by molecular beam epitaxy on bulk AlN{0001}. Compared with the bulk AlN substrate, layers of both polarities feature a suppression of deep-level luminescence, a total absence of the prevalent donor with an exciton binding energy of 28 meV, and a much increased intensity of the emission from free excitons. The dominant donor in these layers is characterized by an associated exciton binding energy of 13 meV. The observation of excited exciton states up to the exciton continuum allows us to directly extract the Γ_5 free exciton binding energy of 57 meV.

© 2023 Author(s). All article content, except where otherwise noted, is licensed under a Creative Commons Attribution (CC BY) license (<http://creativecommons.org/licenses/by/4.0/>). <https://doi.org/10.1063/5.0158390>

INTRODUCTION

The ultra-wide gap semiconductor AlN was first synthesized over a century ago,¹ but it has only recently been recognized that the unique physical properties of AlN make it of great interest for applications in novel electronic and optoelectronic devices. Apart from its direct bandgap of 6.095 eV corresponding to an emission wavelength of 203 nm, most noteworthy are its large piezoelectric coefficients (1.5 C/m² or 5 pm/V),² its high breakdown-field (>10 MV/cm),^{3,4} and its high thermal conductivity (>300 W/mK).⁵ Moreover, AlN has an exciton binding energy exceeding twice the value of kT at room temperature,⁶ which is notably higher than in any other III-V semiconductor with the exception of hBN.⁷ These properties make AlN an attractive material for applications in high-power and millimeter-wave electronics^{8–10} as well as

deep-ultraviolet (UV-C) light emission and lasing.^{11–14} The large exciton binding energy in AlN is also of high interest for the study of the fundamental science of excitons and their condensation.¹⁵

This potential of AlN lay dormant until very recently, when researchers succeeded in synthesizing large AlN crystals of high structural perfection with low dislocation densities (<10⁴–10⁶ cm⁻²) utilizing either physical vapor transport (PVT)^{16–19} for bulk growth or hydride vapor phase epitaxy (HVPE)²⁰ for fabricating thick free-standing layers. The availability of AlN substrates has enabled studies of the fundamental properties of AlN, particularly regarding its spontaneous emission, yielding insights into valence-band ordering, spin-orbit and crystal-field splitting, spin exchange interaction, exciton binding energies, and the detection of impurities and defects. These investigations have been performed by either photo- or cathodoluminescence spectroscopy on PVT-grown

bulk crystals,^{16–19} HVPE-grown free-standing substrates,²⁰ or homoepitaxial AlN layers grown by metal-organic chemical vapor deposition.^{18,21–25}

Numerous studies have focused on the excitonic near-bandedge emission of AlN, resolving transitions due to lowest-energy free excitons with $\Gamma_7^- \otimes \Gamma_{7+}^+$ symmetry (often called A-excitons)²⁶ and several bound exciton transitions.^{23,27} At higher excitation densities, bi-exciton emission (M-band), inelastic exciton–exciton scattering bands (P-bands), and electron–hole plasma recombination were observed.^{17,22} Spectra recorded over a wider spectral range revealed the presence of deep luminescence bands in the range of 2–4 eV that frequently dominate over the near-bandedge emission in terms of integrated intensity. The actual origin of these ubiquitous deep luminescence bands is unknown, but it is generally believed to be related to complexes of native defects, particularly Al vacancies, with impurities such as Si and O that form DX centers in AlN. However, other native defects and the impurity C have been suspected to play an important role in the transitions that give rise to these deep bands.^{6,16,19}

In general, the incorporation of impurities and the formation of native point defects are related in a complex way to the particular growth method and conditions. Surprisingly, there seem to be no detailed studies of the spontaneous emission of homoepitaxial AlN films grown by molecular beam epitaxy (MBE). Furthermore, the point defect incorporation and formation often strongly depends on the bonding configuration on the growth front, i.e., its crystallographic orientation, as reported, for example, for GaN.²⁸ To the best of our knowledge, all of the available studies on the excitonic emission of AlN have been performed on films grown along the Al-polar ([0001]), semi-polar, or non-polar ($[1\bar{1}00]$ and $[1\bar{2}10]$) directions. However, N-polar ($[000\bar{1}]$) (In,Ga)N/(Al,Ga)N heterostructures are of particular interest because they exhibit internal electrostatic fields opposite to those of their metal-polar counterparts, which is considered favorable for various advanced device concepts.²⁹

In the present work, we use cathodoluminescence (CL) spectroscopy in a scanning electron microscope (SEM) to analyze and compare N- and Al-polar homoepitaxial strain-free AlN films grown by MBE in terms of their near-bandedge (around 6 eV) and deep-level (2–4 eV) light emission. With respect to the bare substrate, we find that both N-polar and Al-polar films feature a suppression of deep-level luminescence and the total absence of the donor dominating the NBE of the substrate. Furthermore, the intense-free exciton emission in the films under investigation allows us to directly measure an exciton binding energy of 57 meV from the $\Gamma_5^{\eta \rightarrow \infty}$ transition.

EXPERIMENTS

The three samples under investigation were grown in an MBE system equipped with a radio-frequency plasma source for generating active N and solid-source effusion cells for Al. As substrates, we used bulk AlN wafers grown by PVT with a dislocation density of $<10^4 \text{ cm}^{-2}$. The layers were grown at substrate temperatures above 1000 °C under Al-stable conditions. Details on the surface preparation and growth parameters for the MBE growth of Al- and N-polar homoepitaxial AlN layers are given in Refs. 30–33. Samples I and II consist of a 700-nm thick Al-polar and a 900-nm thick N-polar layer, respectively. Sample III consists of a 1- μm thick N-polar AlN

layer that was capped with 6.7-nm heteroepitaxial GaN. This GaN cap layer serves as a passivation layer for the AlN surface and also acts as a charge-spreading layer during electron beam excitation. As a reference and for comparison with other studies, a freestanding AlN substrate was used.

The samples were investigated by scanning transmission electron microscopy (STEM) on an aberration-corrected ThermoFisher Spectra 300 CFEG operated at 300 keV to confirm their polarity. STEM samples were prepared using a ThermoFisher Helios G4 UX Focused Ion Beam system. Carbon and platinum protective layers were deposited, and a final milling step at 5 keV was used to minimize ion-beam damage. Additionally, atomic force microscopy (AFM) was performed on an Asylum Cypher AFM microscope in tapping mode for sample areas of $2 \times 2 \mu\text{m}^2$ and $20 \times 20 \mu\text{m}^2$. Furthermore, the concentrations of O, C, and Si were measured by time-of-flight secondary ion mass spectrometry (ToF-SIMS) performed by Evans Analytical Group. Finally, triple-axis $\omega/2\theta$ x-ray diffraction (XRD) scans across the symmetrical 002 wurtzite reflection were measured using a Panalytical Empyrean x-ray diffractometer equipped with a PIXcel^{3D} detector and Xe proportional detector. The monochromator consists of a hybrid two-bounce Ge220 crystal utilizing Cu $K\alpha_1$ radiation.

To analyze and compare the optical properties of these samples, low-temperature emission spectra were recorded by CL spectroscopy in a Zeiss Ultra55 SEM equipped with a He-cryo-stage allowing sample temperatures down to 10 K and a Gatan MonoCL4 detection system. The spectrometer is operated with two gratings, one blazed at 300 nm with 2400 grooves/mm (Fig. 2) and the other blazed at 250 nm with 1200 grooves/mm (Fig. 3), resulting in a spectral resolution of ~ 0.0035 and 0.007 eV for a slit width of 0.1 mm, respectively. Note that the line widths of the near-bandedge transitions are limited by this spectral resolution. The monochromator was calibrated using an Hg(Ar) spectral calibration lamp. The error of this calibration amounts to ± 2 Å because of the spectral separation between the highest energy line of the lamp and the AlN near-bandedge emission. The samples were aligned with respect to the detection setup such that mostly light propagating parallel to the *c*-axis, $\mathbf{k} \parallel \mathbf{c}$, and electric field polarization (*E*) orthogonal to the *c*-axis, $\mathbf{E} \perp \mathbf{c}$, was collected. The light was detected monochromatically with a photomultiplier tube (PMT) while stepping through the spectral range, and the spectra were converted to energy scale by a Jacobian transformation, taking into account the refractive index dispersion of air.³⁴ For the CL measurements, all of the AlN samples were sputter coated with 3 nm of Ti to reduce charging effects in the SEM.

RESULTS AND DISCUSSION

Figure 1 summarizes data pertaining to the structural and morphological properties of our AlN layers as well as to their purity. The polarity of the layers is examined by high-angle annular dark-field STEM (HAADF-STEM) as shown in Figs. 1(a) and 1(b), respectively. The yellow spheres in the overlaid ball-and-stick model of the wurtzite crystal structure represent Al atoms, and the white spheres represent N atoms, confirming the nominal polarity of the layers (growth direction pointing upward). Figures 1(c) and 1(d) depict $2 \times 2 \mu\text{m}^2$ atomic force topographs of the *c*-plane surface of the as-grown layers. The trains of well-resolved monolayer steps are

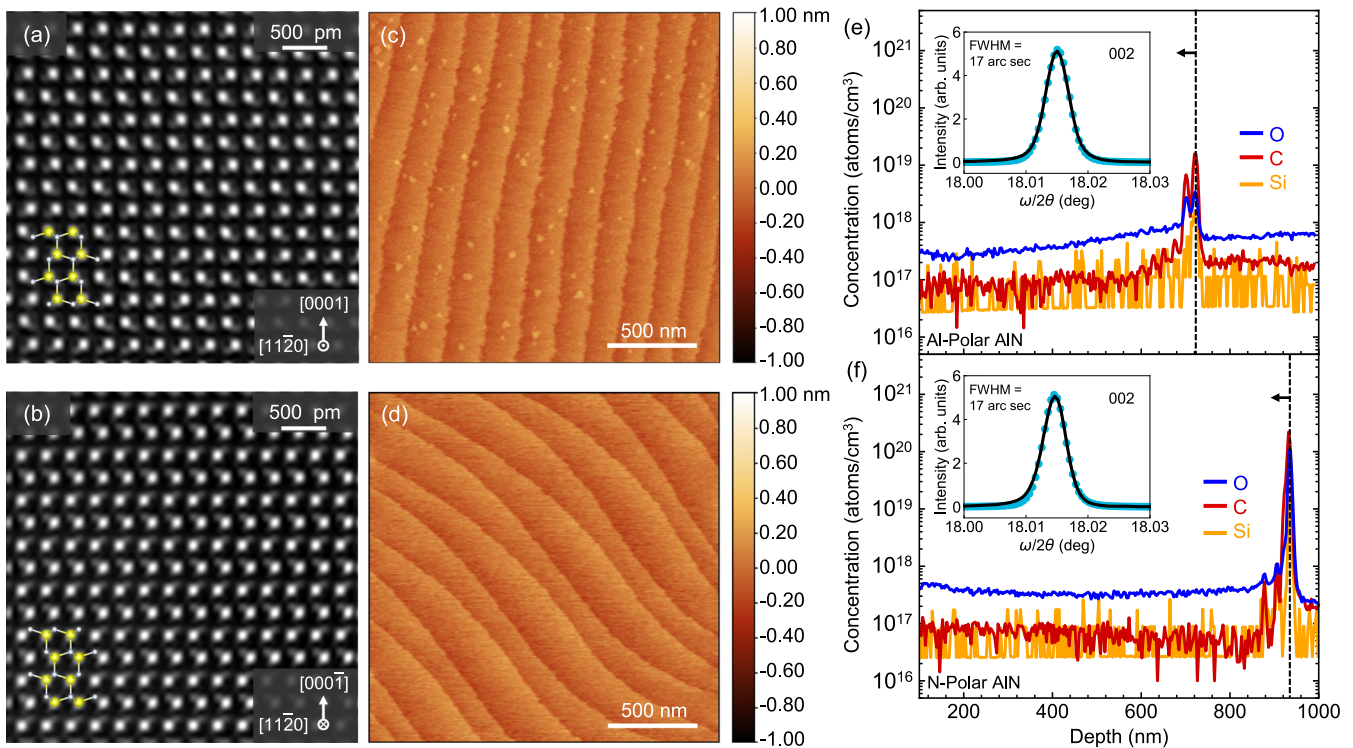


FIG. 1. [(a) and (b)] HAADF-STEM images with overlaid wurtzite ball-and-stick model, [(c) and (d)] c-plane atomic force topographs, and [(e) and (f)] SIMS profiles of samples I (Al-polar AlN, top row) and II (N-polar AlN, bottom row). The insets in figures (e) and (f) show the respective $\omega/2\theta$ x-ray diffraction scans across the 002 reflection of the MBE layers (blue, dotted) and the bare AlN substrate (solid, black).

characteristic of step-flow growth, resulting in a root-mean-square roughness as low as 80 and 160 pm, respectively. Figures 1(e) and 1(f) display ToF-SIMS data for the respective samples revealing comparatively low impurity concentrations for layers of either polarity. The level of [Si] $< 5 \times 10^{16} \text{ cm}^{-3}$ is at and the levels of O and C are close to the detection limit (given in parentheses): [O] $\approx 3 - 4 \times 10^{17} \text{ cm}^{-3}$ ($1 \times 10^{17} \text{ cm}^{-3}$) and [C] $\approx 7 - 8 \times 10^{16} \text{ cm}^{-3}$ ($5 \times 10^{16} \text{ cm}^{-3}$). Hydrogen (not shown) has a concentration below the detection limit for both samples, [H] $< 3 \times 10^{17} \text{ cm}^{-3}$. Note that the spike at the substrate/MBE interface is less pronounced for the Al-polar sample (near 700 nm depth) than for the N-polar sample (near 900 nm depth). This is likely due to a greater adsorption efficiency of impurities on the N-polar surface,^{35,36} as well as the less extensive ex-situ chemical treatment for the N-polar face, as it is more reactive.^{30,32,33} Finally, the insets in Figs. 1(e) and 1(f) depict $\omega/2\theta$ x-ray diffraction scans across the 002 reflection for the Al- and N-polar AlN samples (blue, dotted) compared with the bare AlN substrates they were grown on (solid, black). The line widths of ~ 17 arcsec confirm that the MBE-grown AlN layers are free of strain. The absence of strain is further confirmed by reciprocal space maps around the asymmetric $\bar{1}05$ reflection for Samples I and II (see Fig. S1 in the supplementary material). Symmetric and asymmetric ω scans recorded for Samples I and II exhibit widths between 20 and 30 arcsec, comparable with or below that measured on the corresponding bulk AlN substrates (see Fig. S2 in the supplementary material). For the structural

characterization and SIMS data of sample III, we refer to Figs. S3–S5 in the supplementary material.

CL spectra of samples I and II are compared with one of the bare PVT-AlN substrate (N-polar face) in Fig. 2. An acceleration voltage of 7 keV was used to excite the samples, ensuring that electron-hole pairs are generated only within the homoepitaxial layers (in the first few hundred nm from the AlN/air interface, see Fig. S7 in the supplementary material). Figure 2(a) shows the low-temperature, high-resolution near-bandedge emission spectra normalized to their peak intensities. For all three samples, a distinct high-energy line is observed at $(6.038 \pm 0.005) \text{ eV}$, with the error due to the uncertainty of the wavelength calibration. This transition energy is close to the average energy (6.041 eV) reported for the exciton spin triplet with Γ_5 symmetry in bulk (strain-free) AlN.^{17,21–23,25,27}

For AlN, the negative crystal-field splitting causes the Γ_{7+}^v band to be the uppermost valence band,³⁷ resulting in exciton states of $\Gamma_7^c \otimes \Gamma_{7+}^v$ symmetry (often called A-excitons).³⁸ Spin-exchange interaction splits these states into excitons with the irreducible representation $\Gamma_1 \oplus \Gamma_2 \oplus \Gamma_5$, with the Γ_5 spin triplet being the only optically active state that satisfies $\mathbf{E} \perp \mathbf{c}$ and $\mathbf{k} \parallel \mathbf{c}$, i.e., our measurement geometry. It should be noted that there currently is no consensus in the literature on the assignment of the experimentally observed emission lines and thus the ordering of the $\Gamma_{1}^{\text{H}=1}$ and $\Gamma_{5}^{\text{H}=1}$ states. In fact, researchers have reported both negative^{17,22,23,25,39} and

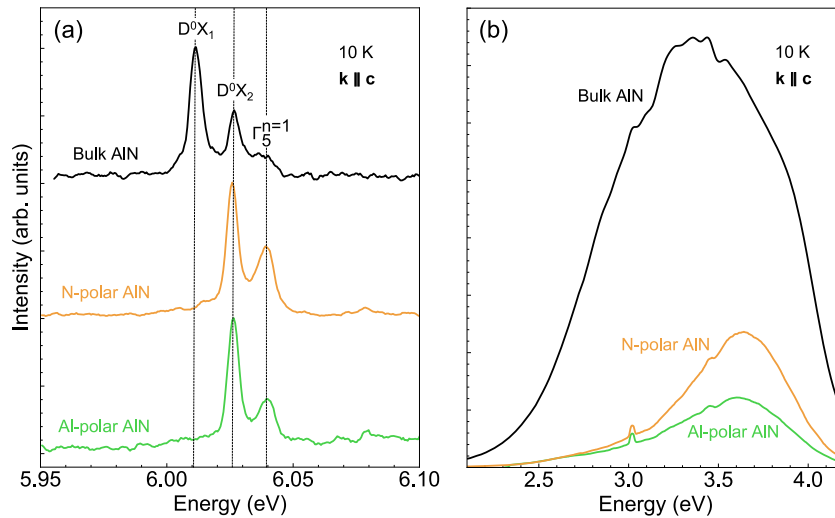


FIG. 2. (a) Low-temperature, high-resolution near-bandedge and (b) deep-level CL spectra for the bare PVT-AlN substrate, as well as samples I and II. The light was collected with $k \parallel c$. The narrow feature just above 3 eV in (b) is the second order of the near-bandedge emission.

positive^{18,20,40–42} values for the spin-exchange splitting j . A possible explanation of this apparent discrepancy is the fact that j depends sensitively on strain.^{26,43,44} For the case of GaN, Paskov *et al.*²⁶ calculated the dependence of the $\Gamma_1^{n=1} - \Gamma_5^{n=1}$ splitting (which is given by $2j$) on biaxial strain and observed that it changes sign for a biaxial compressive strain as small as 2×10^{-4} . The scatter of a lattice

constants of bulk AlN amount to a variation of $\pm 2.5 \times 10^{-4}$ with respect to the strain-free value,⁴⁵ which, in analogy to GaN, may already be sufficient to result in a significant change of the spin-exchange splitting in AlN. An explicit calculation as done by Paskov *et al.*²⁶ for GaN is required to see if this hypothesis can account for the conflicting results in the literature.

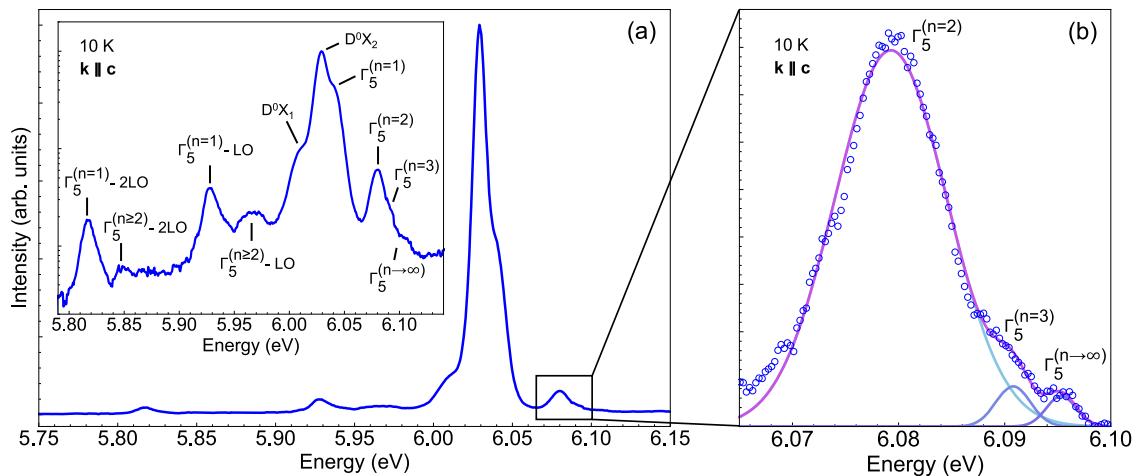


FIG. 3. (a) Low-temperature, high-resolution near-bandedge CL spectrum for sample III on a linear and logarithmic (inset) intensity scale. The integration time was chosen to be $10 \times$ longer than that for the spectra in Fig. 2. (b) Expanded view of the excited free exciton transitions, with $\Gamma_5^{n=2}$, $\Gamma_5^{n=3}$, and $\Gamma_5^{n \rightarrow \infty}$ resolved. The line is a fit of the data with three Gaussians (also shown).

The data in the present work, which are obtained on strain-free AlN, support a negative value of j and thus a lower energy for the Γ_1 compared with the Γ_5 exciton. The geometry ($\mathbf{k} \parallel \mathbf{c}$) of the measurements depicted in Figs. 2 and 3 is compatible with the detection of the Γ_5 , but not the Γ_1 exciton. This fact is confirmed by comparison to measurements taken on the cross-section of sample I (see Fig. S6 in the supplementary material). In the emission normal to the cross-section ($\mathbf{k} \perp \mathbf{c}$), we observe a superposition of the $\Gamma_5^{n=1}$ and $\Gamma_1^{n=1}$ excitons as expected from the selection rules. The intense emission of the $\Gamma_1^{n=1}$ exciton is situated at 6.031 eV, in between the $\Gamma_5^{n=1}$ and D^0X_2 lines. The additional peak observed at higher energy (6.08 eV) for the homoepitaxial layers is attributed to the first excited state of the free Γ_5 exciton as discussed in more detail for sample III.

For the PVT substrate, two intense and narrow lines are observed at 28 and 13 meV below the $\Gamma_5^{n=1}$ free exciton ground state. The former of these lines is absent for both samples I and II. These lines have been frequently observed in previous work and are attributed to donor-bound exciton transitions. D^0X_1 , with an exciton binding energy of 28 meV, has been tentatively assigned to either O²³ or Si²⁷ as the shallow donor, whereas the D^0X_2 with a binding energy of 13 meV has been speculated to be related to a native shallow donor.²³ The dominance of the D^0X_1 line in the spectra of the substrate, and the total absence of this transition in our epitaxial layers, implies a significantly lower concentration of the responsible shallow donor in the layers compared with the substrate. Accordingly, it is unlikely that this line is related to O, the concentration of which is even slightly higher in the layers than in the substrate [cf. Figs. 1(e) and 1(f)]. Si, in contrast, is below the detection limit for all samples, and it is thus possible that the actual concentration in the layers is much below that in the substrate. Our experiments are thus consistent with Si being the donor related to the D^0X_1 line, adding support to the assignments made in Refs. 20, 27, and 46.

To probe radiative deep levels, we performed CL measurements with lower resolution in the range of 2–4.2 eV as shown in Fig. 2(b). All spectra in this figure are normalized to their respective near-bandedge peak intensities. The integrated intensity of the broad luminescence bands observed in this spectral range exceeds the near-bandedge intensity by a factor of 2.5 for the bulk AlN substrate, but it is lower by factors of 0.5 and 0.8 for samples I and II, respectively. Apart from the higher intensity, the CL band from the substrate is much broader and seems to comprise two individual contributions, with the one at higher energy matching the energy of the band in samples I and II. The line shape of samples I and II are almost identical, suggesting that similar types of defects are incorporated for both polarities.

The overall similarity between the radiative properties of the Al- and N-polar AlN samples is remarkable. In contrast, studies on N-polar GaN layers, regardless of whether being grown by MBE or MOCVD, have shown that it is difficult to obtain layers with purity and emission characteristics equivalent to their Ga-polar counterparts. A higher incorporation efficiency of impurities as well as lower formation energy for N vacancies in N-polar GaN growth are discussed as possible reasons for this difference in material quality.⁴⁷ Consequently, N-rich growth seems to be a prerequisite to suppress the formation of N vacancies for GaN(0001̄).²⁸ For AlN, our data show that the situation is much more favorable, suggesting that we

may use the alignment of the polarization fields as an additional degree of freedom for the design of AlN-based light-emitters. Note, however, that interface recombination may become important in group-III nitride heterostructures and may strongly depend on their polarity.^{48–50}

To further elucidate the details of the near-bandedge emission, we turn to sample III, which exhibits the highest emission intensity of all samples. Figure 3(a) shows its low-temperature CL spectrum, collected at an acceleration voltage of 11 keV (still exciting mostly the homoepitaxial layer, see Fig. S7 in the supplementary material). The higher beam energy ensures a high signal intensity, facilitating the reliable detection of weak transitions. As seen best in the inset, ten transitions are resolved, the energies of which are compiled in Table I. The highest energy transitions associated with excited states of the free exciton are better visible in the magnified view displayed in Fig. 3(b). Where available, our values are in good agreement with those of previous studies. In particular, the $E(\Gamma_5^{n=1})$ exciton and its excited states are resolved at 6.038, 6.079, 6.091, and 6.095 eV, together with their longitudinal optical (LO) phonon replicas at lower energies. Again, the D^0X_2 transition and a weak D^0X_1 line (originating from the substrate) contribute to the spectra as well. The prominent transition at 6.079 eV can be readily assigned to the $E(\Gamma_5^{n=2})$ transition, for which energy separations of 37–43 meV with respect to the $E(\Gamma_5^{n=1})$ transition have been reported by other groups,^{17,18,21–23,27,51} although no values are available for the higher-order transitions.

To identify the origin of the transitions at 6.091 and 6.095 eV, we first consider the hydrogenic effective-mass approximation, in which the energies of the excited states as well as the binding energy

TABLE I. Low-temperature (10 K) near-bandedge transitions in AlN. Transitions resolved in the homoepitaxial, N-polar AlN layers measured in the present work are highlighted in bold. All of these values have an experimental uncertainty of ± 1 meV. We also provide the shift with respect to the $\Delta E(\Gamma_5^{n=1})$ transitions and, where available, corresponding literature values. An extended version of this table is provided in the supplementary material.

Transition	E (eV)	$\Delta E(\Gamma_5^{n=1})$ (meV)	$\Delta E_{\text{lit}}(\Gamma_5^{n=1})$ (meV)
$\Gamma_5^{n=1} - \mathbf{2LO}$	5.815	−223	−225, ²² −231 ²⁰
$\Gamma_5^{n \geq 2} - \mathbf{2LO}$	5.849	−189	−188 ²²
$\Gamma_5^{n=1} - \mathbf{LO}$	5.926	−112	−109, ²² −117 ²⁰
$\Gamma_5^{n \geq 2} - \mathbf{LO}$	5.965	−73	−73 ²²
D^0X_α			−37 ²⁵
D^0X_1	6.010	−28	−28, ²⁵ −28.5, ²¹ −28.5 ²⁷
D^0X_β			−25 ²⁵
D^0X_γ			−22.1, ¹⁷ −22.4, ²³ −22.5 ²⁷
D^0X_δ			−19, ²⁵ −19.0 ²⁷
D^0X_2	6.025	−13	−13, ²⁵ −13.3, ²⁷ −13.6 ²¹
D^0X_ϵ			−9.5, ²¹ −9.5 ²⁷
$\Gamma_1^{n=1}$	6.031	−7	−8 ²⁵
$\Gamma_5^{n=1}$	6.038	0	0
$\Gamma_1^{n=2}$			+31 ²⁵
$\Gamma_5^{n=2}$	6.079	+41	+39.4, ²¹ +39.4, ²⁷ +41 ²⁵
$\Gamma_5^{n=3}$	6.091	+53	
$\Gamma_5^{n \rightarrow \infty}$	6.095	+57	

of the free exciton can be determined based on the 1S–2S splitting, i.e., the energy difference between the first excited state and the ground state $E(\Gamma_5^{n=2}) - E(\Gamma_5^{n=1})$. Specifically, the energy of the second excited state is predicted to be

$$E(\Gamma_5^{n=3}) = E(\Gamma_5^{n=1}) + \frac{32}{27}[E(\Gamma_5^{n=2}) - E(\Gamma_5^{n=1})]. \quad (1)$$

Similarly, the energy of the $n \rightarrow \infty$ transition is given by

$$E(\Gamma_5^{n \rightarrow \infty}) = E(\Gamma_5^{n=1}) + \frac{4}{3}[E(\Gamma_5^{n=2}) - E(\Gamma_5^{n=1})]. \quad (2)$$

These equations yield values of 6.087 and 6.093 eV for the $\Gamma_5^{n=3}$ and $\Gamma_5^{n \rightarrow \infty}$ transitions, respectively, slightly lower than the transition energies observed.

The simple hydrogenic approximation is not expected to be in perfect agreement with the actual transition energies, since AlN exhibits a notable anisotropy regarding both the reduced exciton mass μ and the relative static permittivity ϵ . This anisotropy is commonly summarized in the form of the anisotropy parameter $\gamma = \epsilon_{\perp}\mu_{\perp}/(\epsilon_{\parallel}\mu_{\parallel})$ with the directions relative to that of the c axis.^{52–55} For values of γ other than 1 or 0, exact analytical expressions for the excitonic levels do not exist. Gil *et al.*⁵⁴ have provided numerical values for the $\Gamma_5^{n=2}$, $\Gamma_5^{n=3}$, and $\Gamma_5^{n \rightarrow \infty}$ transitions, placing them at 6.076, 6.083, and 6.086 eV for $\gamma \approx 1.8$, the value obtained for AlN using the material parameters given in Ref. 55. These energies are systematically lower than those obtained by the simple hydrogen model because $\gamma > 1$, which results in a reduction of the exciton binding energy. In fact, although the effective Rydberg energy $Ry^* = Ry(H) \mu_{\perp}/(\epsilon_{\parallel}\epsilon_{\perp})$ amounts to 59 meV, where $Ry(H) = 13.6$ eV is the ionization energy of the hydrogen atom, the binding energy obtained within the framework of an anisotropic exciton is only 48 meV, as reported previously by Funato *et al.*²¹ Even the experimentally observed 1S–2S splitting of 41 meV only allows for an exciton binding energy of 52 meV, still inconsistent with the highest energy feature observed in Fig. 3(b).

Indeed, for an accurate determination of the exciton binding energy in AlN, Ishii *et al.*⁵⁵ have pointed out that it is crucial to consider not only crystal anisotropy but also exchange and electron–phonon interactions as well. They showed the latter to result in a significantly increased exciton binding energy for the Γ_5 triplet, namely, 64 meV, accompanied by a 1S–2S splitting of 51 meV. Based on our Γ_5 transition energy of 6.038 eV, these values would result in transition energies for the $\Gamma_5^{n=2}$ and $\Gamma_5^{n \rightarrow \infty}$ excitons of 6.089 and 6.102 eV, too large compared with the experimental values. Clearly, the theory has still to be refined to accurately reproduce the excitonic transition energies observed experimentally. Currently, we share the observation in the literature that the hydrogenic approximation still seems to reproduce experimental data best.³⁹ Consequently, we assign the emission lines observed at 6.091 and 6.095 eV to the $n = 3$ and $n \rightarrow \infty$ states of the Γ_5 free exciton. The energy of the $\Gamma_5^{n \rightarrow \infty}$ transition corresponds to the exciton continuum and thus the bandgap of AlN. Therefore, the energy difference between $\Gamma_5^{n=1}$ and $\Gamma_5^{n \rightarrow \infty}$ directly provides the binding energy of the Γ_5 exciton, which thus amounts to 57 meV.

Other experimental values for the free exciton binding energy reported in the literature range from 47 to 67 meV. Those derived by

relying on the 1S–2S spitting^{17,18,21–23,27,51} or the energy difference between the $n = 1$ free exciton transition and the exciton–exciton scattering band P^{∞} ^{17,20} tend to be close to our value, with the average being about 54 meV. The large overall variation may be due to strain effects, sample heating (especially for high-excitation densities), and the large energy splitting between the Γ_1 and Γ_5 excitons.⁵⁵

In addition, the zero-phonon exciton emission, we resolve two longitudinal optical (LO) phonon replicas each for the free exciton state and the excited states from this sample. In Fig. 3(a), the LO phonon replicas are denoted as $\Gamma_5^{(n=1)} - mLO$ and $\Gamma_5^{(n \geq 2)} - mLO$ with $m \in \{1, 2\}$. The energy spacing between the phonon replicas and the main peaks is a multiple of 112 meV, in close agreement with the quantized LO phonon energy at the Γ -point in AlN.⁵⁶

Table I summarizes all near-bandedge transition energies measured for our MBE films. Column E lists the absolute transition energy and column $\Delta E(\Gamma_5^{n=1})$, the energy shift with respect to the ground state exciton energy $\Gamma_5^{n=1}$. Table I also gives values for $\Delta E_{lit}(\Gamma_5^{n=1})$ of other transitions observed in studies in the literature but which are not observed in our films. Note that the actual origin of the D^0X_{α} , D^0X_{β} , D^0X_{γ} , D^0X_{δ} , D^0X_2 , and D^0X_c lines is not yet known. These lines are generally believed to originate from other donor-bound excitons because of their narrow linewidths, but the contribution of acceptor-bound excitons, inelastic scattering processes, or many-body effects cannot be ruled out.^{21,25,27} An extended table of all near-bandedge transitions that have been reported in the literature can be found in the supplementary material (Table ST1).

Finally, it is interesting to discuss the lack of emission from the $n \geq 3$ free exciton states in any previous study. At the first glance, it may appear surprising to see recombination from free carriers at a nominal temperature of 10 K, considering the strong Coulomb interaction in AlN. The fraction of excitons at a given temperature and electron–hole density is governed by Saha’s law⁵⁷ and is predicted to decrease with increasing carrier temperature and increase with increasing electron–hole density below the Mott transition. In the majority of previous studies, the samples were excited with an ArF laser, which delivers intense ns pulses with a low repetition rate and an energy close to the band edge. Due to the low repetition rate, the lowest excitation densities are typically around 50 kW/cm², resulting in a carrier density in the order of 5×10^{17} cm^{−3}. On the other hand, the excess energy delivered per pulse is comparatively low. For the present CL experiments, the situation is the opposite. The continuous-wave excitation by the electron beam facilitates a comparatively low excitation density. In the present case, we estimate a carrier density of not more than 4×10^{16} cm^{−3} for an acceleration voltage of 11 kV, as detailed in the supplementary material.⁵⁸ The carrier temperature, however, is typically rather high, since electron beam creates highly energetic secondary electrons and holes. The cooling of these hot carriers proceeds via the emission of LO phonons, thus creating a nonequilibrium population of hot LO phonons⁵⁹ that in turn heats the carrier distribution by strongly increasing the probability of LO phonon absorption. Indeed, from the high-energy slope of the $\Gamma_5^{(n=1)} - 2LO$ transition,^{57,60} we deduce a carrier temperature of 120 K. With this carrier temperature and excitation density, Saha’s law (See Fig. S8 in the supplementary material) predicts an excitonic fraction of only 0.82, whereas for the carrier density estimated for ArF excitation,

the fraction increases to 0.95 even for the same carrier temperature. These estimates provide a clear physical explanation for the prominence of excited exciton states in our CL experiments.

CONCLUSION

In summary and conclusion, we have investigated the properties of AlN layers grown by plasma-assisted MBE on both the N- and Al-polar faces of bulk AlN substrates. Regardless of polarity, the layers exhibit atomically smooth surfaces, high structural perfection and purity, and feature intense free exciton emission and suppressed emission from bound excitons and deep-level defects. These results highlight the potential of MBE for the growth of UV emitters. The ability to grow N-polar samples without compromising the crystal quality and thus to change the orientation of the polarization fields in AlN adds an additional degree of freedom that can be exploited in the design of MBE-grown deep-UV emitters. Finally, we have shown that the unique excitation conditions in CL spectroscopy facilitate the detection of several excited states of the Γ_5 exciton, including the excitonic continuum, directly yielding the exciton binding energy of 57 meV.

SUPPLEMENTARY MATERIAL

See the supplementary material for reciprocal space maps as well as symmetric and asymmetric ω scans of samples I and II, a detailed characterization of sample III (AFM, XRD, and SIMS), CL spectra measured under different geometries (sample surface and cross-section), a discussion of the generation volume and excitation density in CL spectroscopy, the phase diagram of the coupled exciton-carrier system according to Saha's law, as well as an extended table of the near-bandedge transitions observed in AlN.

ACKNOWLEDGMENTS

The authors thank Chandrashekhhar Savant, Zexuan Zhang, and Shivali Agrawal for helpful discussions. This work was partially supported by the Cornell Center for Materials Research with funding from the NSF MRSEC program (Grant No. DMR-1719875) as well as by ULTRA, an Energy Frontier Research Center funded by the U.S. Department of Energy (DOE), Office of Science, Basic Energy Sciences (BES), under Award No. DE-SC0021230. Further support was granted by the National Science Foundation with Grant Nos. NNCI-2025233, DMR-1539918, RAISE-TAQS 1839196, MRI 1631282, and AFOSR Grant No. FA9550-20-1-0148. Finally, LvD acknowledges the "Deutscher Akademischer Austauschdienst" (DAAD) for funding provided through the Research Internships in Science and Engineering (RISE) Professional Scholarship.

AUTHOR DECLARATIONS

Conflict of Interest

The authors have no conflicts to disclose.

Author Contributions

L. van Deurzen: Conceptualization (lead); Formal analysis (equal); Investigation (lead); Methodology (equal); Visualization (lead);

Writing – original draft (lead). **J. Singhal:** Investigation (supporting). **J. Encomendero:** Investigation (supporting). **N. Pieczulewski:** Investigation (supporting). **C. S. Chang:** Investigation (supporting). **Y. Cho:** Investigation (supporting). **D. A. Muller:** Funding acquisition (equal); Resources (equal). **H. G. Xing:** Funding acquisition (equal); Resources (equal); Writing – review & editing (supporting). **D. Jena:** Funding acquisition (equal); Resources (equal); Writing – review & editing (supporting). **O. Brandt:** Conceptualization (equal); Formal analysis (equal); Funding acquisition (equal); Methodology (equal); Resources (equal); Visualization (supporting); Writing – review & editing (equal). **J. Lähnemann:** Conceptualization (equal); Formal analysis (equal); Funding acquisition (equal); Methodology (equal); Resources (equal); Visualization (supporting); Writing – review & editing (equal).

DATA AVAILABILITY

The data that support the findings of this study are available within the article and its supplementary material. The raw data may be obtained from the corresponding author upon reasonable request.

REFERENCES

- ¹Fr. Briegleb and A. Geuther, "Ueber das Stickstoffmagnesium und die Affinitäten des Stickgases zu Metallen," *Justus Liebigs Ann. Chem.* **123**, 228–241 (1862).
- ²P. Muralt, J. Conde, A. Artieda, F. Martin, and M. Cantoni, "Piezoelectric materials parameters for piezoelectric thin films in GHz applications," *Int. J. Microw. Wireless Technol.* **1**, 19–27 (2009).
- ³D. Khachariya, S. Mita, P. Reddy, S. Dangi, J. H. Dycus, P. Bagheri, M. H. Breckenridge, R. Sengupta, S. Rathkanthiwar, R. Kirste, E. Kohn, Z. Sitar, R. Collazo, and S. Pavlidis, "Record >10 MV/cm mesa breakdown fields in $\text{Al}_{0.85}\text{Ga}_{0.15}\text{N}/\text{Al}_{0.6}\text{Ga}_{0.4}\text{N}$ high electron mobility transistors on native AlN substrates," *Appl. Phys. Lett.* **120**, 172106 (2022).
- ⁴K. Hussain, A. Mamun, R. Floyd, M. D. Alam, M. E. Liao, K. Huynh, Y. Wang, M. S. Goorsky, M. V. S. Chandrashekhhar, G. Simin, and A. Khan, "High figure of merit extreme bandgap $\text{Al}_{0.87}\text{Ga}_{0.13}\text{N}-\text{Al}_{0.64}\text{Ga}_{0.36}\text{N}$ heterostructures over bulk AlN substrates," *Appl. Phys. Express* **16**, 014005 (2023).
- ⁵Z. Cheng, Y. R. Koh, A. Mamun, J. Shi, T. Bai, K. Huynh, L. Yates, Z. Liu, R. Li, E. Lee, M. E. Liao, Y. Wang, H. M. Yu, M. Kushimoto, T. Luo, M. S. Goorsky, P. E. Hopkins, H. Amano, A. Khan, and S. Graham, "Experimental observation of high intrinsic thermal conductivity of AlN," *Phys. Rev. Mater.* **4**, 044602 (2020).
- ⁶T. Koppe, H. Hofsäss, and U. Vetter, "Overview of band-edge and defect related luminescence in aluminum nitride," *J. Lumin.* **178**, 267–281 (2016).
- ⁷T. C. Doan, J. Li, J. Y. Lin, and H. X. Jiang, "Bandgap and exciton binding energies of hexagonal boron nitride probed by photocurrent excitation spectroscopy," *Appl. Phys. Lett.* **109**, 122101 (2016).
- ⁸S. J. Bader, H. Lee, R. Chaudhuri, S. Huang, A. Hickman, A. Molnar, H. G. Xing, D. Jena, H. W. Then, N. Chowdhury, and T. Palacios, "Prospects for wide bandgap and ultrawide bandgap CMOS devices," *IEEE Trans. Electron Devices* **67**, 4010–4020 (2020).
- ⁹A. Hickman, R. Chaudhuri, L. Li, K. Nomoto, S. J. Bader, J. C. M. Hwang, H. G. Xing, and D. Jena, "First RF power operation of AlN/GaN/AlN HEMTs with >3 A/mm and 3 W/mm at 10 GHz," *IEEE J. Electron Devices Soc.* **9**, 121–124 (2021).
- ¹⁰E. Kim, Z. Zhang, J. Encomendero, J. Singhal, K. Nomoto, A. Hickman, C. Wang, P. Fay, M. Toita, D. Jena, and H. G. Xing, "N-polar GaN/AlGaN/AlN high electron mobility transistors on single-crystal bulk AlN substrates," *Appl. Phys. Lett.* **122**, 092104 (2023).
- ¹¹H. Amano, R. Collazo, C. D. Santi, S. Einfeldt, M. Funato, J. Glaab, S. Hagedorn, A. Hirano, H. Hirayama, R. Ishii, Y. Kashima, Y. Kawakami, R. Kirste, M. Kneissl, R. Martin, F. Mehnke, M. Meneghini, A. Ougazzaden, P. J. Parbrook, S. Rajan,

- P. Reddy, F. Römer, J. Ruschel, B. Sarkar, F. Scholz, L. J. Schowalter, P. Shields, Z. Sitar, L. Sulmoni, T. Wang, T. Wernicke, M. Weyers, B. Witzigmann, Y.-R. Wu, T. Wunderer, and Y. Zhang, "The 2020 UV emitter roadmap," *J. Phys. D: Appl. Phys.* **53**, 503001 (2020).
- ¹²Z. Zhang, M. Kushimoto, T. Sakai, N. Sugiyama, L. J. Schowalter, C. Sasaoka, and H. Amano, "A 271.8 nm deep-ultraviolet laser diode for room temperature operation," *Appl. Phys. Express* **12**, 124003 (2019).
- ¹³Z. Zhang, M. Kushimoto, A. Yoshikawa, K. Aoto, C. Sasaoka, L. J. Schowalter, and H. Amano, "Key temperature-dependent characteristics of AlGaN-based UV-C laser diode and demonstration of room-temperature continuous-wave lasing," *Appl. Phys. Lett.* **121**, 222103 (2022).
- ¹⁴L. van Deurzen, R. Page, V. Protasenko, K. Nomoto, H. G. Xing, and D. Jena, "Optically pumped deep-UV multimode lasing in AlGaN double heterostructure grown by molecular beam homoepitaxy," *AIP Adv.* **12**, 035023 (2022).
- ¹⁵V. Ginzburg, *Key Problems of Physics and Astrophysics* (Mir Publishers, Moscow, 1976).
- ¹⁶Q. Zhou, Z. Zhang, H. Li, S. Golovynskiy, X. Tang, H. Wu, J. Wang, and B. Li, "Below bandgap photoluminescence of an AlN crystal: Co-Existence of two different charging states of a defect center," *APL Mater.* **8**, 081107 (2020).
- ¹⁷M. Feneberg, R. A. R. Leute, B. Neuschl, K. Thonke, and M. Bickermann, "High-excitation and high-resolution photoluminescence spectra of bulk AlN," *Phys. Rev. B* **82**, 075208 (2010).
- ¹⁸S. F. Chichibu, K. Hazu, Y. Ishikawa, M. Tashiro, T. Ohtomo, K. Furusawa, A. Uedono, S. Mita, J. Xie, R. Collazo, and Z. Sitar, "Excitonic emission dynamics in homoepitaxial AlN films studied using polarized and spatio-time-resolved cathodoluminescence measurements," *Appl. Phys. Lett.* **103**, 142103 (2013).
- ¹⁹K. Thonke, M. Lamprecht, R. Collazo, and Z. Sitar, "Optical signatures of silicon and oxygen related DX centers in AlN," *Phys. Status Solidi A* **214**, 1600749 (2017).
- ²⁰R. Ishii, T. Nagashima, R. Yamamoto, T. Hitomi, M. Funato, and Y. Kawakami, "Stimulated emission mechanism of aluminum nitride," *Phys. Rev. B* **105**, 205206 (2022).
- ²¹M. Funato, K. Matsuda, R. G. Banal, R. Ishii, and Y. Kawakami, "Homoepitaxy and photoluminescence properties of (0001) AlN," *Appl. Phys. Express* **5**, 082001 (2012).
- ²²R. a. R. Leute, M. Feneberg, R. Sauer, K. Thonke, S. B. Thapa, F. Scholz, Y. Taniyasu, and M. Kasu, "Photoluminescence of highly excited AlN: Biexcitons and exciton-exciton scattering," *Appl. Phys. Lett.* **95**, 031903 (2009).
- ²³M. Feneberg, B. Neuschl, K. Thonke, R. Collazo, A. Rice, Z. Sitar, R. Dalmau, J. Xie, S. Mita, and R. Goldhahn, "Sharp bound and free exciton lines from homoepitaxial AlN," *Phys. Rev. B* **208**, 1520–1522 (2011).
- ²⁴S. F. Chichibu, T. Onuma, K. Hazu, and A. Uedono, "Major impacts of point defects and impurities on the carrier recombination dynamics in AlN," *Appl. Phys. Lett.* **97**, 201904 (2010).
- ²⁵Z. Bryan, I. Bryan, M. Bobea, L. Hussey, R. Kirste, Z. Sitar, and R. Collazo, "Exciton transitions and oxygen as a donor in m-plane AlN homoepitaxial films," *J. Appl. Phys.* **115**, 133503 (2014).
- ²⁶P. P. Paskov, T. Paskova, P. O. Holtz, and B. Monemar, "Spin-exchange splitting of excitons in GaN," *Phys. Rev. B* **64**, 115201 (2001).
- ²⁷B. Neuschl, K. Thonke, M. Feneberg, S. Mita, J. Xie, R. Dalmau, R. Collazo, and Z. Sitar, "Optical identification of silicon as a shallow donor in MOVPE grown homoepitaxial AlN," *Phys. Status Solidi B* **249**, 511–515 (2012).
- ²⁸P. Tatarczak, H. Turski, K. P. Korona, E. Grzanka, C. Skierbiszewski, and A. Wyszomolka, "Optical properties of N-polar GaN: The possible role of nitrogen vacancy-related defects," *Appl. Surf. Sci.* **566**, 150734 (2021).
- ²⁹Z. Q. Li, M. Lestrade, Y. G. Xiao, and S. Li, "Effects of polarization charge on the photovoltaic properties of InGaN solar cells: Effects of polarization charge on photovoltaic properties of InGaN solar cells," *Phys. Status Solidi A* **208**, 928–931 (2011); F. Akyol, D. N. Nath, E. Gür, P. S. Park, and S. Rajan, "N-polar III-nitride green (540 nm) light emitting diode," *Jpn. J. Appl. Phys.* **50**, 052101 (2011); K. Dong, D. Chen, B. Liu, H. Lu, P. Chen, R. Zhang, and Y. Zheng, "Characteristics of polarization-doped N-face III-nitride light-emitting diodes," *Appl. Phys. Lett.* **100**, 073507 (2012); S.-H. Han, D.-Y. Lee, J.-Y. Lim, J. W. Lee, D.-J. Kim, Y. S. Kim, S.-T. Kim, and S.-J. Park, "Effect of internal electric field in well layer of InGaN/GaN multiple quantum well light-emitting diodes on efficiency droop," *Jpn. J. Appl. Phys.* **51**, 100201 (2012); M. H. Wong, S. Keller, N. Dasgupta, D. J. Denninghoff, D. J. Kolluri, S. Brown, D. F. Lu, J. Fichtenbaum, N. A. Ahmadi, E. Singiseti, U. Chini, A. Rajan, S. DenBaars, S. P. Speck, J. S. Mishra, and U. K. Mishra, "N-polar GaN epitaxy and high electron mobility transistors," *Semicond. Sci. Technol.* **28**, 074009 (2013); S.-W. Feng, P.-H. Liao, B. Leung, J. Han, F.-W. Yang, and H.-C. Wang, "Efficient carrier relaxation and fast carrier recombination of N-polar InGaN/GaN light emitting diodes," *J. Appl. Phys.* **118**, 043104 (2015); L. van Deurzen, S. Bharadwaj, K. Lee, V. Protasenko, H. Turski, H. G. Xing, and D. Jena, "Enhanced efficiency in bottom tunnel junction InGaN blue LEDs," *Proc. SPIE* **11706**, 30–35 (2021); Y. Cho, S. Bharadwaj, Z. Hu, K. Nomoto, U. Jahn, H. G. Xing, and D. Jena, "Blue (In,Ga)N light-emitting diodes with buried n+-p+ tunnel junctions by plasma-assisted molecular beam epitaxy," *Jpn. J. Appl. Phys.* **58**, 060914 (2019); S. Bharadwaj, J. Miller, K. Lee, J. Lederman, M. Siekacz, H. G. Xing, D. Jena, C. Skierbiszewski, and H. Turski, "Enhanced injection efficiency and light output in bottom tunnel-junction light-emitting diodes," *Opt. Express*, **28**, 4489–4500 (2020); K. Lee, S. Bharadwaj, Y.-T. Shao, L. van Deurzen, V. Protasenko, D. A. Muller, H. G. Xing, and D. Jena, "Light-emitting diodes with AlN polarization-induced buried tunnel junctions: A second look," *Appl. Phys. Lett.* **117**, 061104 (2020); S. Bharadwaj, K. Lee, K. Nomoto, A. Hickman, L. van Deurzen, V. Protasenko, H. G. Xing, and D. Jena, "Bottom tunnel junction blue light-emitting field-effect transistors," *ibid.* **117**, 031107 (2020).
- ³⁰Y. Cho, C. S. Chang, K. Lee, M. Gong, K. Nomoto, M. Toita, L. J. Schowalter, D. A. Muller, D. Jena, and H. G. Xing, "Molecular beam homoepitaxy on bulk AlN enabled by aluminum-assisted surface cleaning," *Appl. Phys. Lett.* **116**, 172106 (2020).
- ³¹K. Lee, Y. Cho, L. J. Schowalter, M. Toita, H. G. Xing, and D. Jena, "Surface control and MBE growth diagram for homoepitaxy on single-crystal AlN substrates," *Appl. Phys. Lett.* **116**, 262102 (2020).
- ³²J. Singhal, J. Encomendero, Y. Cho, L. van Deurzen, Z. Zhang, K. Nomoto, M. Toita, H. G. Xing, and D. Jena, "Molecular beam homoepitaxy of N-polar AlN on bulk AlN substrates," *AIP Adv.* **12**, 095314 (2022).
- ³³Z. Zhang, Y. Hayashi, T. Tohei, A. Sakai, V. Protasenko, J. Singhal, H. Miyake, H. G. Xing, D. Jena, and Y. Cho, "Molecular beam homoepitaxy of N-polar AlN: Enabling role of aluminum-assisted surface cleaning," *Sci. Adv.* **8**, eabo6408 (2022).
- ³⁴J. Lähnemann, J. F. Orri, E. Prestat, H. W. Ánes, D. Johnstone, and N. Tappy, "Lumispy v0.2.1," Zenodo. <https://doi.org/10.5281/zenodo.4640445>
- ³⁵H. Ye, G. Chen, Y. Zhu, and S.-H. Wei, "Asymmetry of adsorption of oxygen at Wurtzite AlN (0001) and (000T) surfaces: First-principles calculations," *Phys. Rev. B* **77**, 033302 (2008).
- ³⁶M. S. Miao, P. G. Moses, J. R. Weber, A. Janotti, and C. G. V. Van de Walle, "Effects of surface reconstructions on oxygen adsorption at AlN polar surfaces," *Europhys. Lett.* **89**, 56004 (2010).
- ³⁷J. Li, K. B. Nam, M. L. Nakarmi, J. Y. Lin, H. X. Jiang, P. Carrier, and S.-H. Wei, "Band structure and fundamental optical transitions in wurtzite AlN," *Appl. Phys. Lett.* **83**, 5163–5165 (2003).
- ³⁸K. Cho, "Unified theory of symmetry-breaking effects on excitons in cubic and Wurtzite structures," *Phys. Rev. B* **14**, 4463–4482 (1976).
- ³⁹M. Feneberg, M. Fátima Romero, B. Neuschl, K. Thonke, M. Röppischer, C. Cobet, N. Esser, M. Bickermann, and R. Goldhahn, "Negative spin-exchange splitting in the exciton fine structure of AlN," *Appl. Phys. Lett.* **102**, 052112 (2013).
- ⁴⁰R. Ishii, M. Funato, and Y. Kawakami, "Long-range electron-hole exchange interaction in aluminum nitride," *Phys. Rev. B* **102**, 155202 (2020).
- ⁴¹S. F. Chichibu, K. Kojima, K. Hazu, Y. Ishikawa, K. Furusawa, S. Mita, R. Collazo, Z. Sitar, and A. Uedono, "In-plane optical polarization and dynamic properties of the near-band-edge emission of an m-plane freestanding AlN substrate and a homoepitaxial film," *Appl. Phys. Lett.* **115**, 151903 (2019).
- ⁴²R. Ishii, M. Funato, and Y. Kawakami, "Huge electron-hole exchange interaction in aluminum nitride," *Phys. Rev. B* **87**, 161204 (2013).
- ⁴³T. Koda and D. W. Langer, "Splitting of exciton lines in Wurtzite-type II-VI crystals by uniaxial stress," *Phys. Rev. Lett.* **20**, 50–53 (1968).
- ⁴⁴O. Akimoto and H. Hasegawa, "Strain-induced splitting and polarization of excitons due to exchange interaction," *Phys. Rev. Lett.* **20**, 916–918 (1968).
- ⁴⁵D. Nilsson, E. Janžén, and A. Kakanakova-Georgieva, "Lattice parameters of AlN bulk, homoepitaxial and heteroepitaxial material," *J. Phys. D: Appl. Phys.* **49**, 175108 (2016).

- ⁴⁶B. Neuschl, K. Thonke, M. Feneberg, R. Goldhahn, T. Wunderer, Z. Yang, N. M. Johnson, J. Xie, S. Mita, A. Rice, R. Collazo, and Z. Sitar, "Direct determination of the silicon donor ionization energy in homoepitaxial AlN from photoluminescence two-electron transitions," *Appl. Phys. Lett.* **103**, 122105 (2013).
- ⁴⁷T. K. Zywiets, J. Neugebauer, and M. Scheffler, "The adsorption of oxygen at GaN surfaces," *Appl. Phys. Lett.* **74**, 1695–1697 (1999).
- ⁴⁸S. Fernández-Garrido, J. Lähnemann, C. Hauswald, M. Korytov, M. Albrecht, C. Chèze, C. Skierbiszewski, and O. Brandt, "Comparison of the luminous efficiencies of Ga- and N-polar $\text{In}_x\text{Ga}_{1-x}\text{N}/\text{In}_y\text{Ga}_{1-y}\text{N}$ quantum wells grown by plasma-assisted molecular beam epitaxy," *Phys. Rev. Appl.* **6**, 034017 (2016).
- ⁴⁹C. Chèze, F. Feix, J. Lähnemann, T. Flissikowski, M. Kryško, P. Wolny, H. Turski, C. Skierbiszewski, and O. Brandt, "Luminescent N-polar (In,Ga)N/GaN quantum wells achieved by plasma-assisted molecular beam epitaxy at temperatures exceeding 700 °C," *Appl. Phys. Lett.* **112**, 022102 (2018).
- ⁵⁰T. Auzelle, C. Sinito, J. Lähnemann, G. Gao, T. Flissikowski, A. Trampert, S. Fernández-Garrido, and O. Brandt, "Interface recombination in Ga- and N-polar GaN/(Al,Ga)N quantum wells grown by molecular beam epitaxy," *Phys. Rev. Appl.* **17**, 044030 (2022).
- ⁵¹H. Murotani, T. Kuronaka, Y. Yamada, T. Taguchi, N. Okada, and H. Amano, "Temperature dependence of excitonic transitions in a-plane AlN epitaxial layers," *J. Appl. Phys.* **105**, 083533 (2009).
- ⁵²A. Baldereschi and M. G. Diaz, "Anisotropy of excitons in semiconductors," *Nuovo Cimento B* **68**, 217–229 (1970).
- ⁵³E. A. Muljarov, A. L. Yablonskii, S. G. Tikhodeev, A. E. Bulatov, and J. L. Birman, "Hyperspherical theory of anisotropic exciton," *J. Math. Phys.* **41**, 6026–6041 (2000).
- ⁵⁴B. Gil, D. Felbacq, B. Guizal, and G. Bouchitté, "Excitonic states and their wave functions in anisotropic materials: A computation using the finite-element method and its application to AlN," *Phys. Status Solidi B* **249**, 455–458 (2012).
- ⁵⁵R. Ishii, M. Funato, and Y. Kawakami, "Effects of strong electron–hole exchange and exciton–phonon interactions on the exciton binding energy of aluminum nitride," *Jpn. J. Appl. Phys.* **53**, 091001 (2014).
- ⁵⁶V. Yu. Davydov, Yu. E. Kitaev, I. N. Goncharuk, A. N. Smirnov, J. Graul, O. Semchinova, D. Uffmann, M. B. Smirnov, A. P. Mirgorodsky, and R. A. Evarestov, "Phonon dispersion and Raman scattering in hexagonal GaN and AlN," *Phys. Rev. B* **58**, 12899–12907 (1998).
- ⁵⁷S. Bieker, T. Henn, T. Kiessling, W. Ossau, and L. W. Molenkamp, "Spatially resolved thermodynamics of the partially ionized exciton gas in GaAs," *Phys. Rev. Lett.* **114**, 227402 (2015).
- ⁵⁸U. Jahn, V. M. Kaganer, K. K. Sabelfeld, A. E. Kireeva, J. Lähnemann, C. Pfüller, T. Flissikowski, C. Chèze, K. Biermann, R. Calarco, and O. Brandt, "Carrier diffusion in GaN: A cathodoluminescence study. I. Temperature-Dependent generation volume," *Phys. Rev. Appl.* **17**, 024017 (2022).
- ⁵⁹P. Lugli, C. Jacoboni, L. Reggiani, and P. Kocevar, "Monte Carlo algorithm for hot phonons in polar semiconductors," *Appl. Phys. Lett.* **50**, 1251–1253 (1987).
- ⁶⁰S. Bieker, T. Kiessling, W. Ossau, and L. W. Molenkamp, "Correct determination of low-temperature free-exciton diffusion profiles in GaAs," *Phys. Rev. B* **92**, 121201(R) (2015).